Sulfide Boosting Near-Unity Photoluminescence Quantum Yield of Silver Nanocluster

Shan-Shan Zhang,[†] Shana Havenridge,[‡] Chengkai Zhang,[†] Zhi Wang,[†] Lei Feng,[†] Zhi-Yong Gao,[§] Christine M. Aikens,[‡] Chen-Ho Tung,[†] and Di Sun[*,†]

[†]School of Chemistry and Chemical Engineering, State Key Laboratory of Crystal Materials, Shandong University, Ji'nan, 250100, People's Republic of China.

[‡]Department of Chemistry, Kansas State University, Manhattan, Kansas 66506, USA.

[§]School of Chemistry and Chemical Engineering, Henan Normal University, Xinxiang, 453007, People's Republic of China.

ABSTRACT: Silver nanoclusters have emerged as promising candidates for optoelectronic applications, but their room-temperature photoluminescence quantum yield (PLQY) is far from ideal to access cutting-edge device performance. Herein, two supertetrahedral silver nanoclusters with high PLQY in non-degassed solution at room temperature were constructed by interiorly supporting the core with multiple VO_4^{3-} and E^{2-} anions as structure directing agents, and exteriorly protecting the core with a rigid ligand shell of $PhC{\equiv}C^-$ and $Ph_2PE_2^-$ (E = S, **Ag64-S**; E = Se, **Ag64-Se**). Both clusters have similar outer Ag_{58} tetrahedral cages and $[Ag_6E_4@(VO_4)_4]$ cores, forming a pair of comparable clusters to decrypt the origin of such a high PLQY, particularly in **Ag64-S**, where the PLQY reached up to 97%. The stronger suppression effect of inner sulfides for non-radiative decay is critical to boost the PLQY to near unity. Transient absorption spectroscopy are employed to confirm the phosphorescence nature. The quadruple-capping assembly mechanism involving Ag_7 secondary building units on Ag_{36} truncated tetrahedron was also established by collision induced dissociation studies. This work not only provides a strategy of core engineering for the controlled syntheses of silver nanoclusters with high PLQY, but also deciphers the origin of a near-unity PLQY, which lays a foundation for fabricating highly fluorescent silver nanoclusters in the future.

INTRODUCTION

An overwhelming diversity of silver nanoclusters with distinct physicochemical properties are available for photoluminescence, photochromism, and antibiosis materials.[1-3] Photoluminescence is one of the most important properties of smaller metal nanoclusters; however, it is a great challenge to achieve a bright emission with a high photoluminescence quantum yield (PLQY) for high nuclearity silver clusters at room temperature, which, nevertheless, is one of the primary figures of merit for optoelectronic applications.[4-6] The origin of photoluminescence and various electronic relaxation pathways with respect to the inner metal cores, ligands, and the metal-ligand interfaces have been studied experimentally and theoretically.[7-10] Generally, Ag_2S or Ag_2Se quantum dots, without atomically precise structure, possess high quantum yields,[11-15] while coinage metal nanoclusters usually possess a low PLQY, especially for high nuclearity silver nanoclusters. Nevertheless, the lack of stable atomically precise structures hampers the understanding of emission mechanisms and the rational design to improve PLQY. Although a series of methods have been performed to improve the PLQY of metal nanoclusters,[16-21] such as doping with a hetero metal, rigidifying the surface of the nanocluster, aggregation-induced emission, tailoring the surface structures, embedding nanoclusters into polymers, and dissolving the nanocluster in viscous solvents, achieving intrinsically high PLQY or even boosting PLQY at the atomic level is a huge challenge.

The prerequisite for improving PLQY is to understand the excited states and dissect the radiative and nonradiative decay pathways[22-24] in atomically precise silver nanoclusters. One of the key reasons for using atomically precise nanoclusters is that they possess discrete energy transitions rather than a large manifold of states or energy bands such as those found in a bulk material. In this regard, considerable effort has been paid in the preparation of such nanoclusters.[16-21] Using a rigid ligand is undoubtedly a good strategy to improve PLQY by forming more non-covalent interactions between the ligands (e.g. $\pi\cdots\pi$ and C-H$\cdots\pi$ interactions) that can promote the radiative transitions.[25,26] Heterometallic doping can dramatically spike PLQY in some systems, but the doping position and fraction are difficult to control experimentally, so the mechanism is difficult to determine.[16,27] Previous work reported that confining a few-atom silver nanocluster in Linde Type A (LTA) zeolites greatly improved their luminescence properties, but no structural information was provided.[28] Inspired by this, confining a silver core by a rigid outer metallic framework, ligand shell, or anion passivation shell may be an effective stratgy to boost the PLQY of silver nanocluster.[18,29]

Recent studies have found that the combination of multiple anions can also be used as structure directing agent (SDA), especially tetrahedral templates (MO_4^{n-}), to collaboratively achieve hierarchical structures through solution self-assembly.[30-37] Further, the insertion of small anions such as halide or chalcogenide can segregate the silver core from the shell, producing core-shell silver clusters.[38-41] The most interesting class is the introduction of additional S^{2-} or Se^{2-} ions

in $[AgS_4@Ag_{36}]$, effectively enlarging the inner core from tetrahedral AgS_4[42] to Ag_6Z_4 (E = S/Se)[43]. The larger Ag_6Z_4 core results in the emission maxima from 515 nm to 760 nm and 765 nm for $[Ag_6S_4@Ag_{36}]$ and $[Ag_6Se_4@Ag_{36}]$, respectively. Thus, intervening the formation of metal core by adjusting simple anions in the early stage of assembly may be a feasible way to change the overall structure. These structural features, in turn, contribute to the variances in photoluminescence properties.

Here, the multiple anion template strategy was successfully implemented to synthesize two novel supertetrahedral nanoclusters $[Ag_6E_4@(VO_4)_4@Ag_{58}(PhC{\equiv}C)_{28}(Ph_2PE_2)_{12}]^{4+}$ (E = S, **Ag64-S**; E = Se, **Ag64-Se**). Rigid ligands that could be used as sulfur or selenium releasing reagents were deliberately chosen. Both have been known to lead to high PLQY in non-degassed solution at room temperature; in particular, **Ag64-S** achieves a PLQY up to nearly 100% compared to the most reported coinage metal clusters.[44] While the large core-ligand framework prevents easy accessibility to theoretical information about the emissive excited states, density-functional theory (DFT) calculations show that the electronic transitions that make up the optical peaks of these clusters have charge transfer character between the p orbitals in the S/Se atoms with d character from the Ag outer core atoms and π orbitals in the aromatic rings. As the clusters share a similar size and shape, the origin of higher PLQY in **Ag64-S** can be associated with differences in geometric and optical properties between the two clusters.

RESULTS AND DISCUSSION

Scheme 1. Exploration of the synthesis pathway of **Ag64-S** and the changes of photoluminescence as the reaction process proceeds monitored by 365 nm ultraviolet light. M1: the stirring method; M2: the solvothermal method.

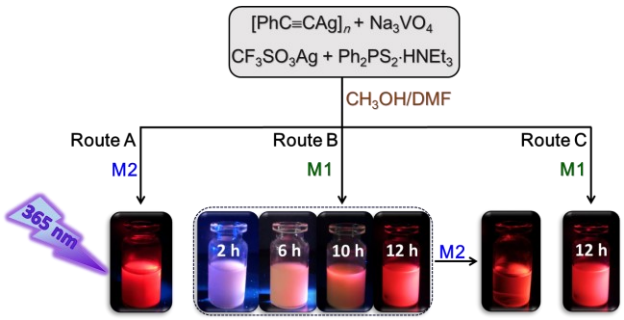

Synthesis Discussion

Three experimental routes were attempted (A-C) to synthesize **Ag64-S** by adding Na_3VO_4, $[PhC{\equiv}CAg]_n$, $Ph_2PS_2{\cdot}HNEt_3$, and CF_3SO_3Ag in MeOH/DMF mixed solvent (Scheme 1 top). Direct solvothermal reaction yields a large amount of red-orange precipitate at the bottom of the glass vial, while the filtrate evaporated to produce red block crystals in a very low yield (<10%, Route A). However, if the solvothermal reaction was performed after stirring 12 h at room temperature, a clear solution was obtained, and the filtrate was evaporated to produce the crystalline target product with an enhanced yield of 46% (Route B). Moreover, the crystals cannot be obtained by stirring alone (Route C). Comparative experiments suggest that stirring can promote the homogeneous mixing of the reactants and facilitate the reaction, but is not conducive to crystallization, whereas the heating-cooling process can promote crystallization. Surprisingly, the extent to which the reaction has progressed can be observed by monitoring the change in luminescence through portable ultraviolet lamp irradiation (Route B). As the stirring reaction proceeds, the purple emission turns to orange-red, signaling that the target product may be slowly generated after 12 h (Scheme 1 bottom). The composition and structure of **Ag64-S** was characterized by single-crystal X-ray diffraction (SCXRD) and electrospray ionization mass spectrometry (ESI-MS). The filtrates obtained by three routes and diluted with CH_2Cl_2 present two prominent peaks in the positive mode ESI-MS. The peak at *m/z* = 3328.7864 (calcd *m/z* = 3328.6385) corresponds to $[Ag_6S_4@(VO_4)_4@Ag_{58}(PhC{\equiv}C)_{28}(Ph_2PS_2)_{12}]^{4+}$ (**1a**) and the other peak at *m/z* = 4487.9290 (cald. *m/z* = 4487.8354) corresponds to $[\mathbf{1a}{+}CF_3SO_3]^{3+}$, which implies that **Ag64-S** has been produced in the filtrate and the counter anion should be $CF_3SO_3^-$ (Figure S1). The orange-red precipitate after reaction (Route A) was washed with ethanol and dissolved in CH_2Cl_2 for ESI-MS analysis; only one significant peak was found at *m/z* = 3328.6273 corresponding to **1a** (Figure S2). For **Ag64-S**, S^{2-} anions were generated in situ by the decomposition of $Ph_2PS_2^-$ ligand, which led to the question: would it be possible to obtain nanoclusters incorporating Se^{2-} if $Ph_2PS_2^-$ was replaced by $Ph_2PSe_2^-$? Therefore, $Ph_2PSe_2{\cdot}K$[45] was designed and synthesized instead of $Ph_2PS_2{\cdot}HNEt_3$ to obtain a similar silver cluster **Ag64-Se** (Scheme S2). As expected, they show different photoluminescence regarding to their emission energy and PLQY. The synthesis, detailed structure diagrams and X-ray diffraction data of these nanoclusters are shown in the Supporting Information (SI).

X-ray Structures of Ag64-S and Ag64-Se

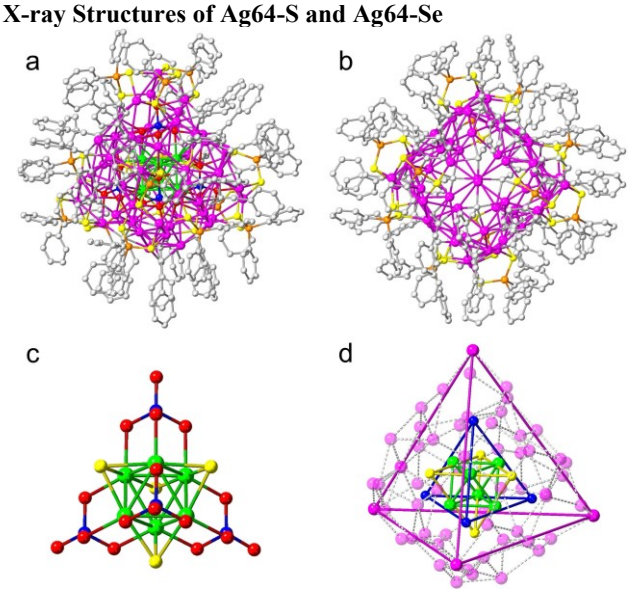

Figure 1. (a) Total cluster structure of **Ag64-S**. (b) The structure of outer metal-ligand shell of $[Ag_{58}(PhC{\equiv}C)_{28}(Ph_2PS_2)_{12}]$ in **Ag64-S**. (c) The structure of $[Ag_6@S_4(VO_4)_4]$ core in **Ag64-S**. (d) The four-shell motif in **Ag64-S** including two silver shells (Ag_6 octahedron: green; Ag_{58} tetrahedron: purple) and two anion shells (VO_4^{3-} tetrahedron: blue; S^{2-} tetrahedron: yellow). Hydrogen atoms are removed for clarity. Color legend: Ag, purple/green; P, orange; S, yellow; V, blue; O, red; C, gray.

The total structures of **Ag64-S** (Figure 1a) and **Ag64-Se** (Figure S5) were determined by the SCXRD at the temperature of 100 K. These clusters crystallized in the hexagonal $P6_3$ space

groups, and their main composition was determined as $[Ag_6@E_4(VO_4)_4@Ag_{58}(PhC{\equiv}C)_{28}(Ph_2PE_2)_{12}]^{4+}$ (E = S, **Ag64-S**; E = Se, **Ag64-Se**). Further, the precise compositions were verified using ESI-MS. Both clusters were successfully isolated with a tetrahedral $[Ag_{58}(PhC{\equiv}C)_{28}(Ph_2PE_2)_{12}]$ shell (Figure 1b), and $[Ag_6@E_4(VO_4)_4]$ core (Figure 1c). Between the inner Ag_6 core and outer Ag_{58} shell, two homocentric tetrahedra are respectively constructed by four chalcogenide atoms (S/Se) and four VO_4^{3-} anions (centered on the V atoms) (Figure 1d). Both clusters are passed by four pseudo-3-fold axes through four apical silver atoms.

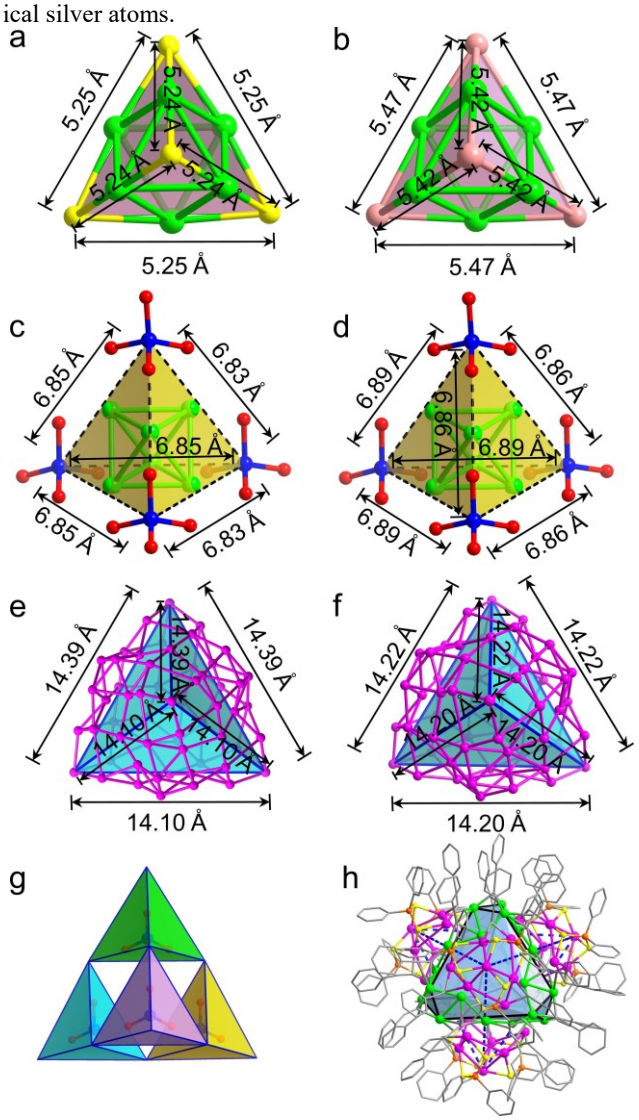

Figure 2. The Ag_6S_4 (a) and Ag_6Se_4 (b) tetrahedral core in **Ag64-S** and **Ag64-Se**. Tetrahedra constructed by four VO_4^{3-} in **Ag64-S** (c) and **Ag64-Se** (d). The metal skeletal structures of Ag_{58} cage of **Ag64-S** (e) and **Ag64-Se** (f). (g) The T*2* supertetrahedral structure of **Ag64-S**. (h) Four $[Ag_7(Ph_2PE_2)_3(PhC{\equiv}C)_3]$) subunits covering the truncated tetrahedron $[Ag_{30}(PhC{\equiv}C)_{16}]$. Hydrogen atoms are removed for clarity. Color legend: Ag, purple/green; P, orange; S, yellow; Se, pink; V, blue; O, red; C, gray.

In order to understand both clusters more comprehensively, the structure from the inner Ag_6 core to outer Ag_{58} metal-ligand shell was analyzed. The four silver trigons of the innermost Ag_6 octahedron capped by four E^{2-} ions form the E_4 tetrahedron and the remaining four are capped by four VO_4^{3-} anions, which finally assemble the $[Ag_6@E_4(VO_4)_4]$ core. Each E^{2-} ion adopts a μ_6 coordination mode to link the outer Ag_{58} cage and inner Ag_6 octahedron (Figure S6) through Ag-S/Se bonding (Ag-S: 2.62-2.64 Å, Ag-Se: 2.70-2.78 Å). The edge lengths of the Se_4 tetrahedron in **Ag64-Se** (5.45 Å) is longer than the S_4 tetrahedron in **Ag64-S** (5.25 Å) due to the fact that atomic radius of Se is larger than S (Figure 2a and 2b), which thus gives a slightly larger Ag_6 core for **Ag64-Se** (Ag···Ag in Ag_6: 2.90-2.91 Å for **Ag64-S** and 2.92-2.94 Å for **Ag64-Se**). Further, four VO_4^{3-} anions (centered on the V atoms) construct an additional tetrahedron that connects the inner Ag_6 octahedron and outer Ag_{58} cage through the μ_4 O atoms bonding with Ag atoms (Ag-O: 2.36-2.80 Å for **Ag64-S** and 2.31-2.80 Å for **Ag64-Se**, Figure S7). The two tetrahedra constructed by VO_4^{3-} have almost identical edge lengths (Figure 2c and 2d). The innermost Ag_6 octahedron and the outer Ag_{58} tetrahedron are connected by Ag-S/Se bonding, Ag-O bonding and Ag···Ag interactions[46] (Ag···Ag: 3.23-3.37 Å for **Ag64-S** and 3.25-3.37 Å for **Ag64-Se**).

Encapsulating the $[Ag_6@E_4(VO_4)_4]$ core, for both clusters, is a $[Ag_{58}(PhC{\equiv}C)_{28}(Ph_2PE_2)_{12}]$ shell with a tetrahedral configuration. As shown in Figure 2e and 2f, two edges of the Ag_{58} cage (average distance of Ag···Ag is 3.00 Å for both) are almost equal. Alternatively, the Ag_{58} cage can be viewed a T*2* supertetrahedral nanocluster which consists of four vertex-shared silver tetrahedra, each of which has one VO_4^{3-} anion in the cavity (Figure 2g). The tetrahedral arrangement and bonding characteristics of VO_4^{3-} anions in the interior dominate the geometry of silver nanoclusters, shaping Ag_{58} a tetrahedron, which fully confirms that the VO_4^{3-} anions can act as an SDA to influence the conformation of the clusters. Alternatively, each vertex of the tetrahedral Ag_{58} cage can be regarded as an $[Ag_7(Ph_2PE_2)_3(PhC{\equiv}C)_3]$ cluster, which are face-capped on four hexagons of a truncated tetrahedron $[Ag_{30}(PhC{\equiv}C)_{16}]$ (Figure 2h).

Two types of ligands regioselectively cover the surface of the Ag_{58} cage. The 28 $PhC{\equiv}C^-$ ligands contain four in μ_3-η^1:η^1:η^1 and 24 in μ_4-η^1:η^1:η^1:η^1 coordination modes, which are divided into four identical groups with each capping on the convex face of the Ag_{58} tetrahedron (Ag-C: 2.09-2.49 Å for **Ag64-S** and 2.09-2.50 Å for **Ag64-Se**), while 12 $Ph_2PE_2^-$ are evenly anchored to the four vertexes of the Ag_{58} tetrahedron in the μ_4-η^2:η^2 coordination mode (Ag-S: 2.49-2.61 Å, Ag-Se: 2.58-2.70 Å, Figure S8). The regioselective distribution of $PhC{\equiv}C^-$ and $Ph_2PE_2^-$ ligands on the exterior solidifies the Ag_{58} tetrahedron.

Solution stability and gas-phase fragmentation

Mass spectrometry is a complementary technique with respect to SCXRD to determine the composition, the charge state, and the solution behaviors of nanoclusters. Various types of mass spectrometric techniques, such as electrospray ionization mass spectrometry (ESI-MS), matrix-assisted laser desorption/ionization mass spectrometry (MALDI-MS), and cold-spray ionization mass spectrometry (CSI-MS), *etc.* have been used in the study of nanoclusters.[47-50] Single crystals of **Ag64-S** and **Ag64-Se** were dissolved in CH_2Cl_2 and subjected to mass spectrometry measurements. Both of them have only one peak in the *m/z* range of 2000-6000 (*m/z* = 3328.6283 for **Ag64-S** and *m/z* = 3656.9846 for **Ag64-Se**). Two peaks are expanded and show a characteristic peak separation of *m/z* = 0.25, confirming a +4 charge state. The predominant peaks were assigned to the molecular ion of **Ag64-S** and **Ag64-Se**, which corresponds to $[Ag_6S_4@(VO_4)_4@Ag_{58}(PhC{\equiv}C)_{28}(Ph_2PS_2)_{12}]^{4+}$ (**1a**) and

$[Ag_6Se_4@(VO_4)_4@Ag_{58}(PhC{\equiv}C)_{28}(Ph_2PSe_2)_{12}]^{4+}$ (**2a**), respectively (Figure 3a and 3b). The results suggest that **Ag64-S** and **Ag64-Se** have high solution stability. In addition, the bond-valence sum (BVS) calculations with the Brese and O'Keeffe method[51] give values of 4.9307-4.9698 (**Ag64-S**) and 4.8098-4.8207 (**Ag64-Se**) for V atoms, which indicates the valences of V atoms are +5. These results jointly confirm that all Ag atoms are in the +1 oxidation state, which is consistent with the long Ag···Ag distances (> 2.88 Å) in the Ag_6 core. After increasing the source voltage and drying temperature, the molecular ion peaks still stands, and no fragmented species are found (Figure S9 and S10). This further confirms that the integrity and stability of these clusters will remain under harsh conditions.

Mass spectrometry is also an important approach to monitor the cluster reaction process and explore possible assembly mechanisms.[52-58] Here, the gas-phase dissociation of **Ag64-S** and **Ag64-Se** is studied using positive-ion mode ESI-MS with varied collision energy (Figure 3c and 3d). The experiments were performed by selecting the specified molecular ion peaks, **1a** and **2a**, colliding them at various energies, respectively, with N_2 gas in collision cell without mass selection by a quadrupole mass filter.

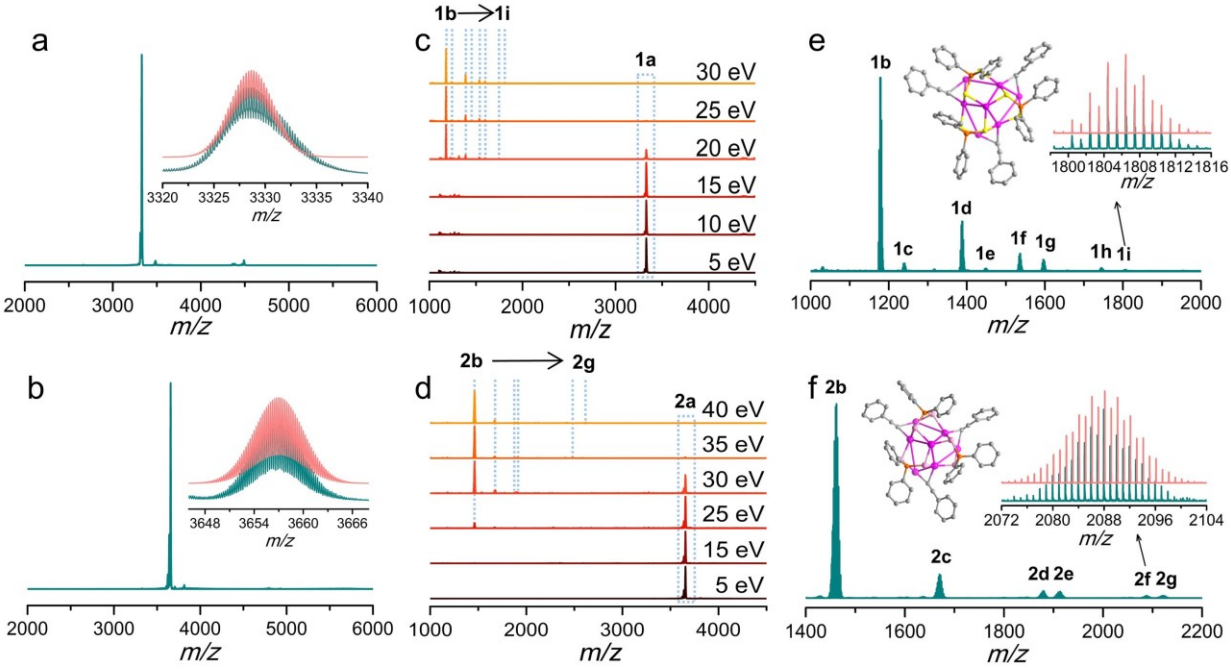

Figure 3. Positive-mode ESI-MS of **Ag64-S** (a) and **Ag64-Se** (b) dissolved in CH_2Cl_2. The insets are experimental (green) and simulated (red) isotopic patterns of **1a** and **2a** species. Positive-mode ESI-MS of **Ag64-S** (c) and **Ag64-Se** (d) collected at different collision energies. Positive-mode ESI-MS of **Ag64-S** (e) at 30 eV collision energy and **Ag64-Se** (f) at 40 eV collision energy. The insets are experimental (green) and simulated (red) isotopic patterns (right) and structures (left) of **1i** and **2f** species.

Scheme 2. The proposed gas phase dissociation pathways for **Ag64-S**. (**1i**: Ag_7 species; **1g**, **1e** and **1h**: Ag_6 species; **1d**, **1c** and **1f**: Ag_5 species; **1b**: Ag_4 species)

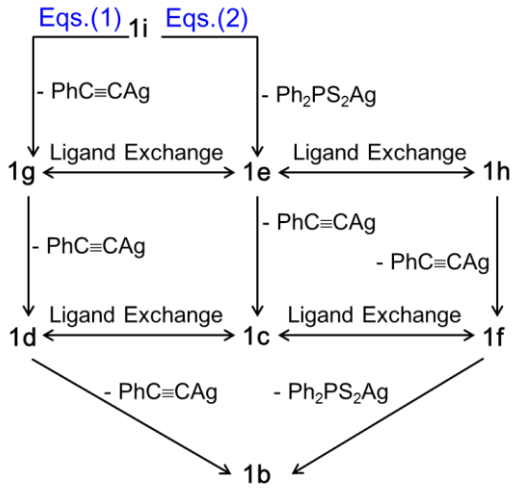

For **Ag64-S**, increasing the collision energy from 5 to 15 eV left the **1a** species intact, suggesting that **Ag64-S** is still stable at low collision energy. Increasing the collision energy to 20 eV, **1a** began to dissociate significantly, and further increasing collision energy to 30 eV resulted in the thorough fragmentation of **1a** into the main species $[Ag_4(Ph_2PS_2)_3]^+$ (**1b**) and some other faint trace species (**1c-1i**) (Figure 3c). A mass spectrum with a collision energy of 30 eV was selected for analysis (Figure 3e). The fragment ions $[Ag_7(PhC{\equiv}C)_3(Ph_2PS_2)_3]^+$ (**1i**) are likely generated through the decomposition of **Ag64-S**. Four fragmented ions **1i**, **1g**, **1d**, and **1b** showed the same *m/z* interval of 207.94, which is equal to the actual mass of PhC≡CAg. Therefore, the **1g**, **1d**, and final **1b** species are sequentially obtained through a core fission pathway from **1i**[59,60] (Eqs. (1) in Scheme 2) and they can be easily assigned to $[Ag_{n+4}(PhC{\equiv}C)_n(Ph_2PS_2)_3]^+$ (n = 2, 1, 0 for **1g**, **1d**, and **1b**, respectively) by good matching of simulated and experimental isotopic distributions (Figure S11 and Table S1). Alternatively, **1i** can decompose to **1e** and **1c** species sequentially through another core fission pathway (Eqs. (2) in Scheme 2). The ligand exchange in paired **1g-1e** and **1e-1h** is similar to that in paired **1d-1c** and **1c-1f**. Furthermore, **1d** and **1f** lost one PhC≡CAg and Ph_2PS_2Ag, respectively, through a core fission pathway to obtain the maximum abundance final product **1b**.

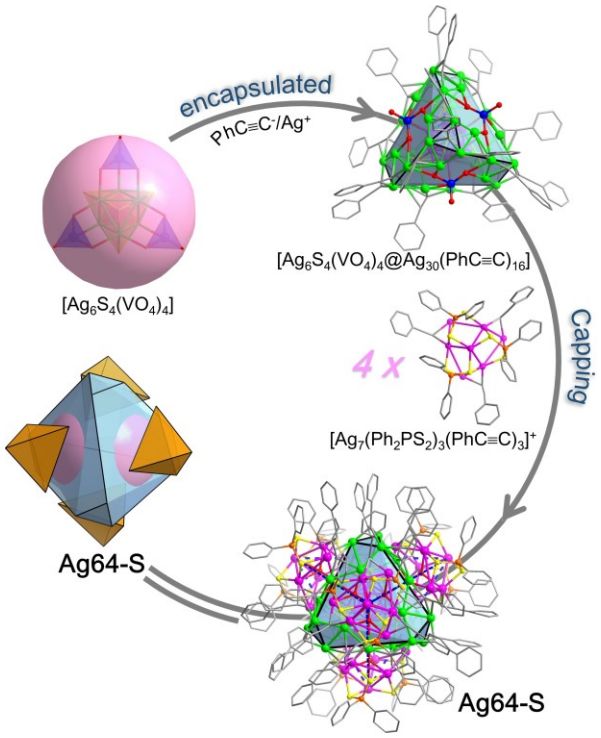

Figure 4 The proposed quadruple-capping assembly route of **Ag64-S**.

All the fragments (**1h-1b**) come from the core fission and ligand exchange of **1i**, so **1i** could be the key component of **Ag64-S**. Incidentally, four **1i** species are located exactly at four vertexes of the Ag_{64} tetrahedron as shown in the X-ray structure, indicating that $[Ag_7(PhC{\equiv}C)_3(Ph_2PS_2)_3]^+$ (**1i**) is an important secondary building unit (SBU) of **Ag64-S**. No other species were observed in mass spectrum, indicating the complete decomposition of **Ag64-S** after removing four SBUs from the four vertexes. The overall fragmentation results in turn reflected the possible quadruple-capping assembly mechanism, that is the inner $[Ag_6@S_4(VO_4)_4]$ transient core may be first formed, then encaged by a $[Ag_{30}(PhC{\equiv}C)_{16}]$ cage to form a $[Ag_6@S_4(VO_4)_4Ag_{30}(PhC{\equiv}C)_{16}]$ truncated tetrahedron where four $[Ag_7(PhC{\equiv}C)_3(Ph_2PS_2)_3]^+$ SBUs are capped on the four faces of it by Ag-O bonding and Ag···Ag interactions (Figure 4).

Similar fragments were also observed for **Ag64-Se** as well (Figure 3d). At the collision energy of 15 eV, fragment ions $[Ag_4(Ph_2PSe_2)_3]^+$ (**2b**) were generated, probably through a core fission pathway. With the collision energy increasing, the intensities of **2b** gradually increased to the maxima at 40 eV; meanwhile, **2a** gradually decreased in intensity and finally disappeared at 40 eV. ESI-MS with a collision energy of 40 eV showed a similar species (**2c-2g**) to **Ag64-S** (Figure 3f). From **2f** to **2d**, **2c**, and final **2b** species, loss of one PhC≡CAg also occurs sequentially through a core fission pathway (Eqs. (1) in Figure S12), and these species can be assigned to $[Ag_{n+4}(PhC{\equiv}C)_n(Ph_2PSe_2)_3]^+$ (n = 3, 2, 1, 0 for **2f**, **2d**, **2c**, **2b**) by good matching of simulated and experimental isotopic distributions (Figure S13 and Table S2). Ligand exchange also exists between **2g** and **2d** species, and then the final product **2b** is obtained from **2g** by losing PhC≡CAg and Ph_2PSe_2Ag in the same way (Eqs. (2) in Figure S12). The similar fragmentation pattern to **Ag64-S** once again confirmed the quadruple-capping assembly mechanism.

Theoretical analysis of Ag64-S and Ag64-Se

Calculations on **Ag64-S** and **Ag64-Se** at the BP86-D3/DZ/COSMO level of theory showed a ground state structure that differs less than 0.20 Å from the crystal structure (Table S3). The optimization contracts the Ag core – Ag core bonds while simultaneously expanding the Ag core – S/Se bonds. One of the more notable geometric changes between the crystal structure and theory happens in the outer protecting cage, where the Ag-S and S-P bonds get larger upon optimization. Despite a longer average bond length between these atoms, the outer cage gets smaller in size with theory as shown by the Ag···Ag bond distances (Figure 2e and 2f). Despite having different atoms, the clusters have essentially the same Ag core – Ag core, Ag core – O, V – O, and V – V average bond distances. The larger differences occur in the inner core and outer shell Ag-S/Se bonds, where the Ag-S bond distances in **Ag64-S** contract by ~0.10 Å compared to the Ag-Se distances in **Ag64-Se**. Further, the S-S, S-P, and Ag-Ag outer cage distances contract by ~0.20 Å compared to the equivalent bonds in **Ag64-Se**.

Ag64-S and **Ag64-Se** both have a superatomic electron count of zero because all Ag atoms are in the +1 oxidation state. The **Ag64-S** and **Ag64-Se** clusters have large HOMO (H) – LUMO (L) gaps of 1.45 eV and 1.32 eV, respectively. The LUMO has large s atomic contributions from Ag which collectively form the 1S orbital (Figure S14). This MO has unique energy placement, sitting 0.44 eV and 0.25 eV below the other unoccupied MOs for **Ag64-S** and **Ag64-Se** respectively (Figure S15). There is another noticeable energetic gap in the virtual MOs between the L+15 and L+16 MOs in **Ag64-S**, as well as the L+12 and L+13 MOs in **Ag64-Se** of 0.11 eV and 0.17 eV respectively. The occupied MOs have very different nature, where there is no superatomic orbitals but rather local atomic contributions. The HOMO in particular has p atomic orbital character localized on the S/Se atoms. Both clusters have close energy gaps in the occupied molecular orbitals (MOs), differing less than 0.08 eV.

The theoretical absorption spectrum (Figure S16) matches the spectral shape of experiment very well. Both theory and experiment predict a lower energy excitation for **Ag64-Se** compared to **Ag64-S**. The theoretical peaks of interest occur at 3.09 eV with an oscillator strength of 3.47 x 10-3 a.u. in **Ag64-S**, and 3.04 eV with an oscillator strength of 3.77 x 10-3 a.u. in **Ag64-Se**. These peaks form collective single particle transitions from the H-46 to the L+26 and H-17 to L+41 in **Ag64-S**, as well as H-117 to L+1 and H-14 to L+48 in **Ag64-Se**. Because the occupied MOs form almost a manifold of states, it is not surprising that transitions do not arise in the frontier orbitals. Further, these orbitals are all comprised of atomic p character from the aromatic rings, p character from the S/Se atoms, as well as some atomic d character from the Ag atoms. The electronic density in these transitions generally resides on the outer cage of these clusters, with hardly any contribution from the core, except in the occupied MOs, where the p atomic orbitals in the S/Se atoms in the inner tetrahedron contribute heavily. The transitions that make up this peak do not overlap in electronic density, hinting that there is charge transfer character from the S/Se atoms and aromatic rings to d character from the outer cage Ag atoms and aromatic groups on a different spatial part of the cluster (Figure S17 and S18). Unfortunately, exchange-correlation functionals such as BP86 do not model charge transfer excitations well in density functional theory (DFT) calculations as they are too local in nature. Long range corrected functionals help to remedy this issue, however, the **Ag64-S** and **Ag64-Se**

clusters are very large for calculations at this higher level of theory. In addition to the peak at 3 eV, there are three other notable absorption peaks in the theoretical spectrum of both clusters at ~2.70 eV, ~2.40 eV, and ~2.10 eV. Similar to the main peak, there is heavy mixing in the transitions that make up these peaks (Table S4). In general, **Ag64-S** blueshifts the absorption peaks compared to **Ag64-Se**, and **Ag64-Se** possesses about 200 more electronic states between the first two peaks but has the same number of electronic states between peak (b) and (c) as well as peak (c) and (d).

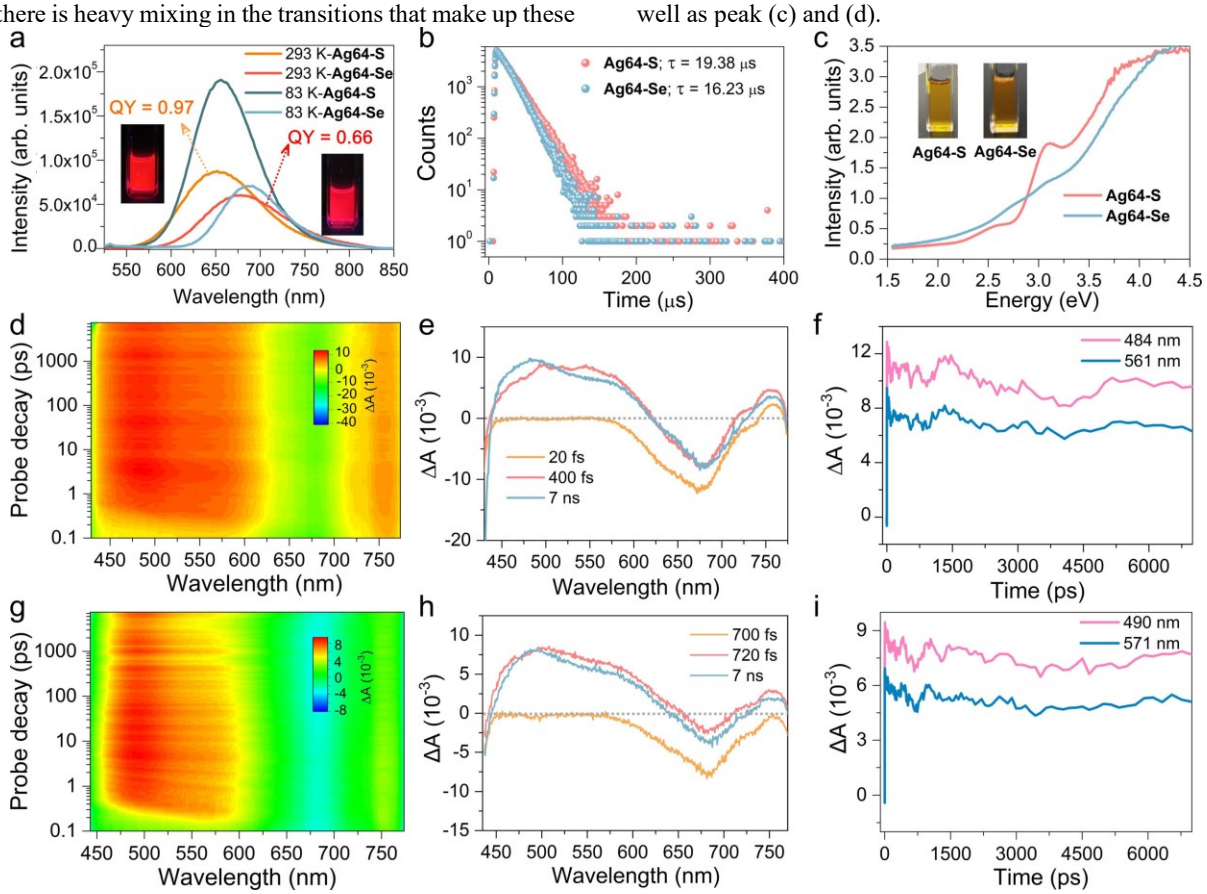

Figure 5. (a) The emission spectra of **Ag64-S** and **Ag64-Se** in CH_2Cl_2 at 293 K and 83 K. Inset: the photographs of **Ag64-S** and **Ag64-Se** taken under 365 nm UV light at 293 K. (b) The microsecond PL decay traces of **Ag64-S** and **Ag64-Se** in CH_2Cl_2 at 293 K. (c) The optical absorption spectra of **Ag64-S** and **Ag64-Se** in CH_2Cl_2. Inset: the photographs of **Ag64-S** and **Ag64-Se** dissolved in CH_2Cl_2, respectively. Map of TA spectra of **Ag64-S** (d) and **Ag64-Se** (g) pump at 400 nm in CH_2Cl_2. TA spectra of **Ag64-S** (e) and **Ag64-Se** (h) at three different time delays. TA kinetics decay of **Ag64-S** (f) and **Ag64-Se** (i) probed at selected wavelengths.

Photoluminescence properties of Ag64-S and Ag64-Se.

Photoluminescence (PL) is amongst the most intriguing and fascinating characteristics of nanoclusters.[4-6] Under UV irradiation, the CH_2Cl_2 solution of **Ag64-S** emits red-orange light with an emission maximum at 650 nm, while **Ag64-Se** emits at 678 nm (Figure 5a). Both tetrahedral clusters are bright emitters in crystalline state, solution, and in frozen glass (Figure S19). Of note, the quantum yields are measured to be 97% and 66%, respectively in non-degassed solution at room temperature (Figure S20). At 83 K, the frozen glass emission maxima red-shifted to 656 and 688 nm for **Ag64-S** and **Ag64-Se**, respectively (Figure 5a). The slight red-shift of them at 83 K should be attributed to the enhancement of argentophilic interactions at low temperature, which leads to the decrease of energy gap between ground and the excited states.[61] The temperature-dependent emission spectra of both clusters from 83 to 293 K are provided in supporting information (Figure S21). The absorption and emission of **Ag64-S** is found at higher energy than that of **Ag64-Se**, which indicates the involvement of S/Se atoms is incredibly important in the excited states (Figure S22). Since Se has more loose binding of lone pair electrons than S, the lower energy gap between ground and excited states related to Se→Ag charge transfer is attributed to the red-shifted emission for **Ag64-Se**.[62]

With reference to previous spectroscopic studies on related Ag/Au-chalcogenide clusters, the emissions are tentatively assigned as derived from triplet states of a ligand-to-metal charge transfer (^{3}LMCT; S/Se→Ag) character mixing with metal-centered (^{3}MC; ds/dp) states which are modified by Ag···Ag interactions.[63-66] For **Ag64-S**, the red-orange emission shows single-exponential behavior with lifetimes at microsecond scale (19.38 μs, 293 K; 28.48 μs, 83 K). Corresponding excited-state lifetimes for **Ag64-Se** are 16.23 and 17.30 μs at 293 K and 83 K, respectively (Figure 5b and Figure S23). The lifetime at microsecond scale and the large Stokes shift (~0.67 eV for **Ag64-S** and ~0.54 eV for **Ag64-Se**) indicate that the emissions are likely to be phosphorescence (Figure 5c).

Ag64-S and **Ag64-Se** with the identical structural motifs provide an ideal platform to reveal the effect of the S/Se atoms on the PL properties. To reveal the key factor affecting PLQY, the rate constants for radiative delay (k_r) and non-radiative delay (k_{nr}) were estimated using equations in Table 1. Comparison of the k_r and k_{nr} values of them suggests that the high PLQY of **Ag64-S** is largely associated with slow non-radiative decay rather than the fast radiative decay.[22] This is reflected by the

shorter average Ag···Ag distances of the Ag_6 core in **Ag64-S** (2.90 Å) than those in **Ag64-Se** (2.93 Å), which is attributed to the stronger confinement effect of the tetrahedron formed by four S atoms than that formed by Se atoms, as reflected by shorter S···S edge length (5.25 Å) than Se···Se (5.45 Å).[28] Therefore, the non-radiation transitions is suppressed by the smaller S_4 tetrahedral shell surrounding the Ag_6 core.

Although optimized S_1 and T_1 calculations for these clusters were not obtained, there are notable properties obtained with theory that contribute to the PL mechanism of these clusters. Initially, as the HL gap is smaller in the optimized ground state structure of **Ag64-Se** compared to **Ag64-S**, it is expected to be smaller in the excited states as well. The lower HL energy gap can be attributed to the red shifted emission in **Ag64-Se** as Se has more loose binding of lone pairs compared to S as discussed in the previous section. Secondly, the MO diagrams show that there is a large separation of the 1S (LUMO) orbital from the unoccupied orbitals, as well as larger separations within higher energy unoccupied orbitals. As large electronic energy gaps between orbitals promote the emission of a photon, this notion hints that if there is non-radiative relaxation out of these states, it will be slow as demonstrated through the Landau-Zener effect.[67,68] Further, the vertical excitations that make up the absorption spectrum hint that the large contribution from the p atomic orbitals on the S/Se atoms in the inner core to a molecular orbital with contribution from d orbitals on the Ag outer cage atoms has charge transfer character. While the exact states that classify this mechanism are unknown, LMCT is qualitatively present with this level of theory.

Table 1. PL parameters of Ag64-S and Ag64-Se

Cluster	QY (%)	τ (μs)	k_r (s^{-1})[b]	k_{nr} (s^{-1})[c]
Ag64-S	97	19.38	5.01×10^4	1.50×10^3
Ag64-Se	66	16.23	4.05×10^4	2.11×10^4
[b]k_r = radiative decay [c]k_{nr} = non-radiative decay	$\tau = \frac{1}{k_r + k_{nr}}$		$QY = \frac{k_r}{k_r + k_{nr}}$	

In order to further understanding the PL mechanism of the **Ag64-S** and **Ag64-Se**, femtosecond transient absorption (TA) measurement were performed to investigate the excited state dynamics. After pumping **Ag64-S** at 400 nm, one broad excited state absorptions (ESA) was immediately observed between 425 and 625 nm (Figures 5d and 5e). However, neither decay nor the rise of ESA was observed during the time window due to the ultrafast intersystem crossing (ISC).[69] The ESA at ~484 and ~561 nm has no obvious decay in the time domain of ~400 fs to 7 ns, which suggests that excited electrons has a long-lived decay, but do not be detected by femtosecond TA (Figure 5f). Combined with microsecond lifetime (19.38 μs) obtained by time-correlated single photon counting, the ESA may originate from the triplet excited state (T_1). This phenomenon also shows that the generation of T_1 is very efficient. For **Ag64-Se**, a broad ESA signal was observed between 450 and 600 nm. Similarly, the ESA signal has almost no decay up to 7 ns (Figure 5i) and also has a microsecond lifetime (16.23 μs). So the TA profiles and relaxation dynamics of **Ag64-Se** suggest that ESA may also belong to T_1 excited state (Figures 5g-5i). The excited electrons from the triplet state go back to the ground state,[23,70] resulting the intrinsic phosphorescence for both of them. In addition, we verified singlet oxygen ($^1O_2$) generation experiments by degrading 1, 3-diphenylisobenzofuran (DPBF), thus demonstrating that both **Ag64-S** and **Ag64-Se** emit phosphorescence (Figure S24).[70]

The unique optical properties with high PLQY imply that these clusters would be great for potential applications. As an additional example to demonstrate the strong PL, a maple leaf was sprayed with a dichloromethane solution of **Ag64-S** as ink. As shown in Figures S25a and 25b, the maple leaf was nearly pale brown in natural light, but it became red and shiny under 365 nm ultraviolet light, indicating that **Ag64-S** could be used as an anti-counterfeit agent. Besides, we selected the high quantum yield **Ag64-S** to fabricate an LED device, by placing the mixture of **Ag64-S** and commercial glue onto an UV LED chip (365 nm) and curing in an oven at 60 °C for 3 h. The LED emits bright orange-red lights at a voltage of 3.0 V (inset left in Figure S25c). The emission spectrum of the orange red-emitting LED is shown in Figure S25c with a peak centered at 656 nm and CIE 1931 chromaticity coordinate at (0.669, 0.331) (inset right in Figure S25c). The application of **Ag64-S** not only expands the source of LED material and anti-counterfeit agent, but also interprets the new function of silver nanoclusters.

CONCLUSIONS

In summary, this work presents two novel supertetrahedral silver nanoclusters constructed synergistically by $PhC{\equiv}C^-$, $Ph_2PS_2^-$ ($Ph_2PSe_2^-$) ligands and VO_4^{3-}, S^{2-} (Se^{2-}) templates. The quadruple-capping assembly mechanism involving four Ag_7 SBUs standing on truncated tetrahedron was confirmed by collision induced dissociation study. The differences between S and Se can be seen by the longer Ag-S/Se and V-V bonds, forming a larger outer cage in **Ag64-Se**, as well as smaller Ag-Ag core bonds compared to **Ag64-S**. Theoretically, the single particle transitions in the absorption spectrum show charge transfer character; however, these results are only qualitative due to the size of the clusters. Both clusters exhibit quite high room-temperature PLQY, which can be applied as luminescence materials. The experimental results reveal that the excited-state transition of S/Se is the fundamental origin for the difference of PL characteristics. Theoretical observation of a 1S LUMO that is well-separated from the other orbitals may explain the high quantum yields observed. The difference of PLQY between **Ag64-S** and **Ag64-Se** is mainly related to the lower non-radiative decay involving S atoms. This work will open a fresh avenue in the construction of new silver nanoclusters with high PLQY by screening multiple simple anionic templates as structure directing agents and using rigid ligands as protective ligands. Further work on modulating the configuration of silver nanoclusters by introducing different anionic templates or ligands to obtain application-oriented silver clusters is in progress.

ASSOCIATED CONTENT

Supporting Information. Experimental details, computational details, detailed crystallographic structure, data including the CIF file, PXRD, IR, EDS mapping, molecular orbital diagrams, absorption details, and electronic density of single particle transitions. This information is available free of charge via the internet at http://pubs.acs.org.

AUTHOR INFORMATION

Corresponding Author

dsun@sdu.edu.cn

ORCID

Di Sun: 0000-0001-5966-1207

Notes

The authors declare no competing financial interest.

ACKNOWLEDGMENT

This work was financially supported by the National Natural Science Foundation of China (Grant Nos. 22171164, 91961105, 22171164, 22150410333), the Fok Ying Tong Education Foundation (171009), the Natural Science Foundation of Shandong Province (Nos. ZR2019ZD45, ZR2020ZD35, JQ201803 and ZR2017MB061), the Taishan Scholar Project of Shandong Province of China (Nos. tsqn201812003 and ts20190908), the Qilu Youth Scholar Funding of Shandong University, Project for Scientific Research Innovation Team of Young Scholar in Colleges and Universities of Shandong Province (2019KJC028), the Fundamental Research Funds of Shandong University (zy202102). S.H. and C.M.A were supported by the National Science Foundation (CHE-1905048) of the United States. The computing for this work was performed on the Beocat Research Cluster at Kansas State University, which is funded in part by NSF grants CHE-1726332, CNS-1006860, EPS-1006860, and EPS-0919443. We also thank Dr. Peng Lu from the School of Physics, Shandong University and Prof. Meng Zhou from University of Science and Technology of China, for the helpful discussions.

REFERENCES

1. Yu, H. Z.; Rao, B.; Jiang, W.; Yang, S.; Zhu, M. Z. The Photoluminescent Metal Nanoclusters with Atomic Precision. *Coord. Chem. Rev.* **2019**, *378*, 595-617.
2. Xie, Y.-P.; Shen, Y.-L.; Duan, G.-X.; Han, J.; Zhang, L.-P.; Lu, X. Silver Nanoclusters: Synthesis, Structures and Photoluminescence. *Mater. Chem. Front.* **2020**, *4* (8), 2205-2222.
3. Yam, V. W.-W.; Au, V. K.-M.; Leung, S. Y.-L. Light-Emitting Self-Assembled Materials Based on d^8 and d^{10} Transition Metal Complexes. *Chem. Rev.* **2015**, *115* (15), 7589-7728.
4. Kang, X.; Zhu, M., Tailoring the photoluminescence of atomically precise nanoclusters. *Chem. Soc. Rev.* **2019**, *48* (8), 2422-2457.
5. Takano, S.; Hirai, H.; Nakashima, T.; Iwasa, T.; Taketsugu, T.; Tsukuda, T., Photoluminescence of Doped Superatoms $M@Au_{12}$ (M = Ru, Rh, Ir) Homoleptically Capped by $(Ph_2)PCH_2P(Ph_2)$: Efficient Room-Temperature Phosphorescence from $Ru@Au_{12}$. *J. Am. Chem. Soc.* **2021**, *143* (28), 10560-10564.
6. Titov, A. A.; Filippov, O. A.; Smol'yakov, A. F.; Godovikov, I. A.; Shakirova, J. R.; Tunik, S. P.; Podkorytov, I. S.; Shubina, E. S. Luminescent Complexes of the Trinuclear Silver(I) and Copper(I) Pyrazolates Supported with Bis(diphenylphosphino)methane. *Inorg. Chem.* **2019**, *58* (13), 8645-8656.
7. Wu, Z.; Jin, R. On the Ligand's Role in the Fluorescence of Gold Nanoclusters. *Nano Lett.* **2010**, *10* (7), 2568-2573.
8. Weerawardene, K. L. D. M.; Aikens, C. M. Origin of Photoluminescence of $Ag_{25}(SR)_{18}^-$ Nanoparticles: Ligand and Doping Effect. *J. Phys. Chem. C* **2018**, *122* (4), 2440-2447.
9. Mustalahti, M.; Myllyperkio, P.; Malola, S.; Lahtinen, T.; Salorinne, K.; Koivisto, J.; Hakkinen, H.; Pettersson, M. Molecule-Like Photodynamics of $Au_{102}(p\text{-MBA})_{44}$ Nanocluster. *ACS Nano* **2015**, *9* (3), 2328-2335.
10. Krishnadas, K. R.; Sementa, L.; Fortunelli, A.; Stener. M.; Fürstenberg, A.; Longhi, G.; Bürgi, T. Chiral Functionalization of an Atomically Precise Noble Metal Cluster: Insights into the Origin of Chirality and Photoluminescence. *ACS Nano* **2020**, *14* (8), 9687-9700.
11. Jiang, P.; Zhu, C.-N.; Zhang, Z.-L.; Tian, Z.-Q.; Pang, D.-W. Water-Soluble Ag_2S Quantum Dots for Near-Infrared Fluorescence Imaging in Vivo. *Biomaterials* **2012**, *33* (20), 5130-5135.
12. Chen, G.; Tian, F.; Zhang, Y.; Zhang, Y.; Li, C.; Wang, Q. Tracking of Transplanted Human Mesenchymal Stem Cells in Living Mice using Near-Infrared Ag_2S Quantum Dots. *Adv. Funct. Mater.* **2014**, *24* (17), 2481-2488.
13. Yu, M.; Yang, X.; Zhang, Y.; Yang, H.; Huang, H.; Wang, Z.; Dong, J.; Zhang, R.; Sun, Z.; Li, C.; Wang, Q. Pb-Doped Ag_2Se Quantum Dots with Enhanced Photoluminescence in the NIR-II Window. *Small* **2021**, *17* (8), 2006111.
14. Hong, G.; Robinson, J. T.; Zhang, Y.; Diao, S.; Antaris, A. L.; Wang, Q.; Dai, H. In Vivo Fluorescence Imaging with Ag_2S Quantum Dots in the Second Near-Infrared Region. *Angew. Chem. Int. Ed.* **2012**, *51* (39), 9818-9821.
15. Du, Y.; Xu, B.; Fu, T.; Cai, M.; Li, F.; Zhang, Y.; Wang, Q. Near-infrared Photoluminescent Ag_2S Quantum Dots from a Single Source Precursor. *J. Am. Chem. Soc.* **2010**, *132* (5), 1470-1471.
16. Soldan, G.; Aljuhani, M. A.; Bootharaju, M. S.; AbdulHalim, L. G.; Parida, M. R.; Emwas, A.-H.; Mohammed, O. F.; Bakr, O. M. Gold Doping of Silver Nanoclusters: A 26-Fold Enhancement in the Luminescence Quantum Yield. *Angew. Chem. In. Ed.* **2016**, *55* (19), 5749-5753.
17. Li, Q.; Zhou, D.; Chai, J.; So, W. Y.; Cai, T.; Li, M.; Peteanu, L. A.; Chen, O.; Cotlet, M.; Gu, X. W.; Zhu, H.; Jin, R. Structural Distortion and Electron Redistribution in Dual-Emitting Gold Nanoclusters. *Nat. Commun.* **2020**, *11* (1), 2897.
18. Han, Z.; Dong, X.-Y.; Luo, P.; Li, S.; Wang, Z.-Y.; Zang, S.-Q.; Mak, T. C. W. Ultrastable Atomically Precise Chiral Silver Clusters with More than 95% Quantum Efficiency. *Sci. Adv.* **2020**, *6* (6), eaay0107.
19. Li, Q.; Mosquera, M. A.; Jones, L. O.; Parakh, A.; Chai, J.; Jin, R.; Schatz, G. C.; Gu, X. W. Pressure-Induced Optical Transitions in Metal Nanoclusters. *ACS Nano* **2020**, *14* (9), 11888-11896.
20. Li, Q.; Zhou, M.; So, W. Y.; Huang, J.; Li, M.; Kauffman, D. R.; Cotlet, M.; Higaki, T.; Peteanu, L. A.; Shao, Z.; Jin, R. A Monocuboctahedral Series of Gold Nanoclusters: Photoluminescence Origin, Large Enhancement, Wide Tunability, and Structure-Property Correlation. *J. Am. Chem. Soc.* **2019**, *141* (13), 5314-5325.
21. Sugiuchi, M.; Maeba, J.; Okubo, N.; Iwamura, M.; Nozaki, K.; Konishi, K. Aggregation-Induced Fluorescence-to-Phosphorescence Switching of Molecular Gold Clusters. *J. Am. Chem. Soc.* **2017**, *139* (49), 17731-17734.
22. Xie, Y.-P.; Shen, Y.-L.; Duan, G.-X.; Han, J.; Zhang, L.-P.; Lu, X. Silver Nanoclusters: Synthesis, Structures and Photoluminescence. *Mater. Chem. Front.* **2020**, *4* (8), 2205-2222.
23. Li, Q.; Zeman, C. J.; Schatz, G. C.; Gu, X. W. Source of Bright Near-Infrared Luminescence in Gold Nanoclusters. *ACS Nano* **2021,** *15* (10), 16095-16105.
24. Chen, S.; Xiong, L.; Wang, S.; Ma, Z.; Jin, S.; Sheng, H.; Pei, Y.; Zhu, M. Total Structure Determination of $Au_{21}(S\text{-Adm})_{15}$ and Geometrical/Electronic Structure Evolution of Thiolated Gold Nanoclusters. *J. Am. Chem. Soc.* **2016**, *138* (34), 10754-10757.
25. Ito, S.; Takano, S.; Tsukuda, T., Alkynyl-Protected $Au_{22}(C{\equiv}CR)_{18}$ Clusters Featuring New Interfacial Motifs and R-Dependent Photoluminescence. *J Phys. Chem. Lett.* **2019**, *10* (21), 6892-6896.
26. Khatun, E.; Ghosh, A.; Chakraborty, P.; Singh, P.; Bodiuzzaman, M.; Ganesan, P.; Nataranjan, G.; Ghosh, J.; Pal, S. K.; Pradeep, T. A thirty-fold Photoluminescence Enhancement Induced by Secondary Ligands in Monolayer Protected Silver Clusters. *Nanoscale* **2018**, *10* (42), 20033-20042.
27. Wang, S.; Meng, X.; Das, A.; Li, T.; Song, Y.; Cao, T.; Zhu, X.; Zhu, M.; Jin, R. A 200-fold Quantum Yield Boost in the Photoluminescence of Silver Doped Ag_xAu_{25-x} Nanoclusters: The 13th Silver Atom Matters. *Angew. Chem. Int. Ed.* **2014**, *53* (9), 2376-2380.
28. Grandjean, D.; Coutino-Gonzalez, E.; Ngo Tuan, C.; Fron, E.; Baekelant, W.; Aghakhani, S.; Schlexer, P.; D'Acapito, F.; Banerjee, D.; Roeffaers, M. B. J.; Minh Tho, N.; Hofkens, J.; Lievens, P. Origin

of the Bright Photoluminescence of few-Atom Silver Clusters Confined in LTA Zeolites. *Science* **2018**, *361* (6403), 686-689.
29. Zhang, S.-S.; Liu, R.-C.; Zhang, X.-C.; Feng, L.; Xue, Q.-W.; Gao, Z.-Y.; Tung, C.-H.; Sun, D. Core Engineering of Paired Core-Shell Silver Nanoclusters. *Sci. China. Chem.* **2021**, *64* (12), 2118-2124.
30. Wang, Z.; Yang, F. L.; Yang, Y.; Liu, Q. Y.; Sun, D. Hierarchical Multi-Shell 66-Nuclei Silver Nanoclusters Trapping Subvalent Ag_6 Kernels. *Chem. Commun.* **2019**, *55* (69), 10296-10299.
31. Wang, Z.; Su, H.-F.; Kurmoo, M.; Tung, C.-H.; Sun, D.; Zheng, L.-S. Trapping an Octahedral Ag_6 Kernel in a Seven-fold Symmetric Ag_{56} Nanowheel. *Nat. Commun.* **2018**, *9* (1), 2094.
32. Liu, J.-W.; Wang, Z.; Chai, Y.-M.; Kurmoo, M.; Zhao, Q.-Q.; Wang, X.-P.; Tung, C.-H.; Sun, D. Core Modulation of 70-Nuclei Core-Shell Silver Nanoclusters. *Angew. Chem. Int. Ed.* **2019**, *58* (19), 6276-6279.
33. Wang, Z.; Qu, Q. P.; Su, H. F.; Huang, P.; Gupta, R. K.; Liu, Q. Y.; Tung, C. H.; Sun, D.; Zheng, L. S. A novel 58-Nuclei Silver Nanowheel Encapsulating a Subvalent Ag_6^{4+} Kernel. *Sci. China. Chem.* **2020**, *63* (1), 16-20.
34. Liu, J.-W.; Feng, L.; Su, H.-F.; Wang, Z.; Zhao, Q.-Q.; Wang, X.-P.; Tung, C.-H.; Sun, D.; Zheng, L.-S. Anisotropic Assembly of Ag_{52} and Ag_{76} Nanoclusters. *J. Am. Chem. Soc.* **2018**, *140*, 1600-1603.
35. Zhou, K.; Geng, Y.; Yan, L. K.; Wang, X. L.; Liu, X. C.; Shan, G. G.; Shao, K. Z.; Su, Z. M.; Yu, Y. N. An Ultrastable $\{Ag_{55}Mo_6\}$ Nanocluster with a Ag-Centered Multishell Structure. *Chem. Commun.* **2014**, *50* (80), 11934-11937.
36. Su, Y. M.; Wang, Z.; Schein, S.; Tung, C. H.; Sun, D. A Keplerian Ag_{90} Nest of Platonic and Archimedean Polyhedra in Different Symmetry Groups. *Nat. Commun.* **2020**, *11* (1), 3316.
37. Wang, Z.; Li, M.-D.; Shi, J.-Y.; Su, H.-F.; Liu, J.-W.; Feng, L.; Gao, Z.-Y.; Xue, Q.-W.; Tung, C.-H.; Sun, D.; Zheng L.-S. In Situ Capture of a Ternary Supramolecular Cluster in a 58-Nuclei Silver Supertetrahedron, *CCS Chem.* **2021**, *3*, 1873-1880.
38. Chen, Z. Y.; Tam, D. Y. S.; Mak, T. C. W. Ethynide-Stabilized high-Nuclearity Silver(I) Sulfido Molecular Clusters Assembled using Organic Sulfide Precursors. *Chem. Commun.* **2016**, *52* (36), 6119-6122.
39. Hau, S. C. K.; Cheng, P. S.; Mak, T. C. W. Enlargement of Globular Silver Alkynide Cluster via Core Transformation. *J. Am. Chem. Soc.* **2012**, *134* (6), 2922-2925.
40. Chen, Z. Y.; Tam, D. Y. S.; Mak, T. C. W. Chloride Assisted Supramolecular Assembly of a Luminescent Gigantic Cluster: $[Ag_{216}S_{56}Cl_7(C{\equiv}CPh)_{98}(H_2O)_{12}]^-$ with Pseudo-T_h Skeleton and Five-Shell Arrangement. *Nanoscale* **2017**, *9* (26), 8930-8937.
41. Anson, C. E.; Eichhöfer, A.; Issac, I.; Fenske, D.; Fuhr, O.; Sevillano, P.; Persau, C.; Stalke, D.; Zhang, J. Synthesen und Kristallstrukturen der ligandenstabilisierten Silberchalkogenidcluster $[Ag_{154}Se_{77}(dppxy)_{18}]$, $[Ag_{320}(S\mathit{t}Bu)_{60}S_{130}(dppp)_{12}]$, $[Ag_{352}S_{128}(S\mathit{t}C_5H_{11})_{96}]$ and $[Ag_{490}S_{188}(S\mathit{t}C_5H_{11})_{114}]$. *Angew. Chem. Int. Ed.* **2008**, *120* (7), 1346-1351.
42. Li, X. Y.; Su, H. F.; Yu, K.; Tan, Y. Z.; Wang, X. P.; Zhao, Y. Q.; Sun, D.; Zheng, L. S. A Platonic Solid Templating Archimedean Solid: an Unprecedented Nanometre-Sized Ag_{37} Cluster. *Nanoscale* **2015**, *7* (18), 8284-8288.
43. Wang, Z.; Liu, J.-W.; Su, H.-F.; Zhao, Q.-Q.; Kurmoo, M.; Wang, X.-P.; Tung, C.-H.; Sun, D.; Zheng, L.-S. Chalcogens-Induced $Ag_6Z_4@Ag_{36}$ (Z = S or Se) Core-Shell Nanoclusters: Enlarged Tetrahedral Core and Homochiral Crystallization. *J. Am. Chem. Soc.* **2019**, *141* (44), 17884-17890.
44. Zhang, M. M.; Dong, X. Y.; Wang, Y. J.; Zang, S. Q.; Thomas, C. W. M. Recent Progress in Functional Atom-Precise Coinage Metal Clusters Protected by Alkynyl Ligands. *Coord. Chem. Rev.* **2022**, *453* (15), 214315.
45. Artem'ev, A. V.; Malysheva, S. F.; Gusarova, N. K.; Trofimov, B. A. Rapid and Convenient One-Pot Method for the Preparation of Alkali Metal Phosphinodiselenoates. *Synthesis* **2010**, *14*, 2463-2467.
46. Schmidbaur, H.; Schier, A. Argentophilic Interactions. *Angew. Chem. Int. Ed.* **2015**, *54* (3), 746-784.
47. Yao, Q.; Yuan, X.; Chen, T.; Leong, D. T.; Xie, J. Engineering Functional Metal Materials at the Atomic Level. *Adv. Mater.* **2018**, *30*, 1802751.
48. Zavras, A.; Ghar, H.; Ariafard, A.; Canty, A. J.; O'Hair, R. A. J. Gas-Phase Ion-Molecule Reactions of Copper Hydride Anions $[CuH_2]^-$ and $[Cu_2H_3]^-$. *Inorg. Chem.* **2017**, *56* (5), 2387-2399.
49. Ma, H. Z.; McKay, A. I.; Mravak, A.; Scholz, M. S.; White, J. M.; Mulder, R. J.; Bieske, E. J.; Bonacic-Koutecky, V.; O'Hair, R. A. J. Structural Characterization and Gas-Phase Studies of the $[Ag_{10}H_8(L)_6]^{2+}$ Nanocluster Dication. *Nanoscale* **2019**, *11*, 22880-22889.
50. Chem, T. K.; Yao, X. F.; Nasaruddin, R. R.; Xie, J. P. Electrospray Ionization Mass Spectrometry: A Powerful Platform for Noble-Metal Nanocluster Analysis. *Angew. Chem. Int. Ed. **2019**, 58 (3),* 11967-11977.
51. O'Keeffe, M.; Brese, N. E. Bond-Valence Parameters for Solids. *Acta Cryst.* **1991**, *B47*, 192-197.
52. Yao, Q.; Fung, V.; Sun, C.; Huang, S.; Chen, T.; Jiang, D. E.; Lee, J. Y.; Xie, J. Revealing Isoelectronic Size Conversion Dynamics of Metal Nanoclusters by a Noncrystallization Approach. *Nat. Commun.* **2018**, *9* (1), 1979.
53. Mashiach, R.; Weissman, H.; Avram, L.; Houben, L.; Brontvein, O.; Lavie, A.; Arunachalam, V.; Leskes, M.; Rybtchinski, B.; Bar-Shir, A. In situ NMR reveals Real-time Nanocrystal Growth Evolution via Monomer-Attachment or Particle-Coalescence. *Nat. Commun.* **2021**, *12* (1), 229.
54. Zhang, B.; Chen, C.; Chuang, W.; Chen, S.; Yang, P. Size Transformation of the $Au_{22}(SG)_{18}$ Nanocluster and Its Surface-Sensitive Kinetics. *J. Am. Chem. Soc.* **2020**, *142* (26), 11514-11520.
55. Han, B. L.; Wang, Z.; Gupta, R. K.; Feng, L.; Wang, S.; Kurmoo, M.; Gao, Z. Y.; Schein, S.; Tung, C. H.; Sun, D. Precise Implantation of an Archimedean $Ag@Cu_{12}$ Cuboctahedron into a Platonic Cu_4Bis(diphenylphosphino)hexane$_6$ Tetrahedron. *ACS Nano* **2021**, *15* (5), 8733-8741.
56. He, W. M.; Zhou, Z.; Han, Z.; Li, S.; Zhou, Z.; Ma, L. F.; Zang, S. Q. Ultrafast Size Expansion and Turn-On Luminescence of Atomically Precise Silver Clusters by Hydrogen Sulfide. *Angew. Chem. Int. Ed.* **2021**, *60* (15), 8505-8509.
57. Du, X.; Chai, J.; Yang, S.; Li, Y.; Higaki, T.; Li, S.; Jin, R. Fusion Growth Patterns in Atomically Precise Metal Nanoclusters. *Nanoscale* **2019**, *11* (41), 19158-19165.
58. Zhang, S.; Li, Y.; Feng, L.; Xue, Q.; Gao, Z.; Tung, C.; Sun, D. Octagold Selenido Nanoclusters: Significance of Surface Ligands on Tuning Geometric and Electronic Structure of Au_8Se_2 Kernel. *Nano Res.* **2021**, *14*, 3343-3351.
59. Robinson, P. S. D.; Nguyen, T.-L.; Lioe, H.; O'Hair, R. A. J.; Khairallah, G. N. Synthesis and gas-phase uni- and bi-molecular Reactivity of Bisphosphine Ligated Gold Clusters, $[Au_xL_y]^{n+}$. *Inter. J. Mass Spectrom.* **2012**, *330-332*, 109-117.
60. Chakraborty, P.; Baksi, A.; Khatun, E.; Nag, A.; Ghosh, A.; Pradeep, T. Dissociation of Gas Phase Ions of Atomically Precise Silver Clusters Reflects Their Solution Phase Stability. *J. Phys. Chem. C* **2017**, *121* (20), 10971-10981.
61. Mirzadeh, N.; Priver, S. H.; Blake, A. J.; Schmidbaur, H.; Bhargava, S. K. Innovative Molecular Design Strategies in Materials Science Following the Aurophilicity Concept. *Chem. Rev.* **2020**, *120* (15), 7551-7591.
62. Wang, Q.-M.; Lee, Y.-A.; Crespo, O.; Deaton, J.; Tang, C.; Gysling, H. J.; Gimeno, M. C.; Larraz, C.; Villacampa, M. D.; Laguna, A.; Eisenberg R. Intensely Luminescent Gold(I)-Silver(I) Cluster Complexes with Tunable Structural Features. *J. Am. Chem. Soc.* **2004**, *126* (31), 9488-9489.
63. Yam, V. W.-W.; Lee, W.-K.; Lai, T.-F. Synthesis and Luminescent Properties of a Novel Tetranuclear Copper(I) Cluster containing a μ_4-Sulfur Moiety. X-Ray Crystal Structure of $[Cu_4(\mu\text{-dppm})_4(\mu_4\text{-S})](PF_6)_2{\cdot}2Me_2CO$ [dppm = bis (diphenylphosphino)methane], *J. Chem. Soc., Chem. Commun*. **1993**, 1571-1573.
64. Forward, J. M.; Bohmann, D.; Fackler, Jr., J. P.; Staples, R. J. Luminescence Studies of Gold(I) Thiolate Complexes. *Inorg. Chem.* **1995**, *34*, 6330-6336.
65. Yam, V. W.-W.; Lo, K. K.-W.; Cheung K.-K. A Novel Luminescent μ_4-Selenido-Bridged Copper(I) Tetramer. *Inorg. Chem.* **1996**, *35* (12), 3459-3462.
66. Yam, V. W.-W.; Cheng, E. C.-C.; Cheung K.-K. A Novel High-Nuclearity Luminescent Gold(I)-Sulfido Complex. *Angew. Chem. Int. Ed.* **1999**, *38* (1-2), 197-199.
67. Leggett, A. J.; Chakravarty, S.; Dorsey, A. T.; Fisher, M. P. A.; Garg, A.; Zwerger, W. Dynamics of the Dissipative Two-State System. *Rev. Mod. Phys.***1987**, *59*, 1.

68. Kayanuma, Y.; Fukuchi, S. On the Probability of Non-adiabatic Transitions in Multiple Level Crossings. *J. Phys. B: At. Mol. Phys.* **1985**, *18*, 4089.
69. Li, Q.; Zhou, D.; Chai, J.; So, W. Y.; Cai, T.; Li, M.; Peteanu, L. A.; Chen, O.; Cotlet, M.; Gu, X. W.; Zhu, H.; Jin, R., Structural Distortion and Electron Redistribution in Dual-emitting Gold Nanoclusters. *Nat. Commun.* **2020**, *11* (1), 2897.
70. Song, Y.; Li, Y.; Zhou, M.; Liu, X.; Li, H.; Wang, H.; Shen, Y.; Zhu, M.; Jin, R., Ultrabright $Au@Cu_{14}$ Nanoclusters: 71.3% Phosphorescence Quantum Yield in Non-degassed Solution at Room Temperature. *Sci. Adv.* **2021**, *7* (2), eabd2091.

Table of Content